

Interannual-decadal variability of wintertime mixed layer depths in the North Pacific detected by an ensemble of ocean syntheses

Article

Accepted Version

Toyoda, T., Fujii, Y., Kuragano, T., Kosugi, N., Sasano, D., Kamachi, M., Ishikawa, Y., Masuda, S., Sato, K., Awaji, T., Hernandez, F., Ferry, N., Guinehut, S., Martin, M., Peterson, K. A., Good, S. A., Valdivieso, M. ORCID: <https://orcid.org/0000-0002-1738-7016>, Haines, K. ORCID: <https://orcid.org/0000-0003-2768-2374>, Storto, A., Masina, S., Kohl, A., Yin, Y., Shi, L., Alves, O., Smith, G., Chang, Y.-S., Vernieres, G., Wang, X., Forget, G., Heimbach, P., Wang, O., Fukumori, I., Lee, T., Zuo, H. and Balmaseda, M. (2017) Interannual-decadal variability of wintertime mixed layer depths in the North Pacific detected by an ensemble of ocean syntheses. *Climate Dynamics*, 49 (3). pp. 891-907. ISSN 0930-7575 doi: <https://doi.org/10.1007/s00382-015-2762-3> Available at <https://centaur.reading.ac.uk/52364/>

It is advisable to refer to the publisher's version if you intend to cite from the work. See [Guidance on citing](#).

Published version at: <http://link.springer.com/article/10.1007%2Fs00382-015-2762-3>

To link to this article DOI: <http://dx.doi.org/10.1007/s00382-015-2762-3>

Publisher: Springer

All outputs in CentAUR are protected by Intellectual Property Rights law, including copyright law. Copyright and IPR is retained by the creators or other copyright holders. Terms and conditions for use of this material are defined in the [End User Agreement](#).

www.reading.ac.uk/centaur

CentAUR

Central Archive at the University of Reading

Reading's research outputs online

1 **Title**

2 Interannual-decadal variability of wintertime mixed layer depths in the North Pacific detected by
3 an ensemble of ocean syntheses.

4

5 **Authors**

6 Takahiro Toyoda, Yosuke Fujii, Tsurane Kuragano, Naohiro Kosugi, Daisuke Sasano, and
7 Masafumi Kamachi (Meteorological Research Institute, Japan Meteorological Agency
8 (MRI/JMA), Tsukuba, Japan)

9 Yoichi Ishikawa (Center for Earth Information Science and Technology, Japan Agency for
10 Marine-Earth Science and Technology (CEIST/JAMSTEC), Yokohama, Japan)

11 Shuhei Masuda, and Kanako Sato (Research and Development Center for Global Change
12 (RCGC), JAMSTEC, Yokohama, Japan)

13 Toshiyuki Awaji (CEIST/JAMSTEC, Yokohama, Japan; Kyoto University, Kyoto, Japan)

14 Fabrice Hernandez (Institut de Recherche pour le Développement (IRD), Toulouse, France;
15 Mercator Océan, Ramonville Sant-Agne, France)

16 Nicolas Ferry (Mercator Océan, Ramonville Sant-Agne, France)

17 Stéphanie Guinehut (Collecte Localisation Satellites (CLS), Ramonville Sant-Agne, France)

18 Matthew Martin, K. Andrew Peterson, and Simon A. Good (Met Office, Exeter, UK)

19 Maria Valdivieso, and Keith Haines (National Centre for Earth Observation (NCEO),
20 Department of Meteorology, University of Reading (U-Reading), Reading, UK)

21 Andrea Storto (Centro Euro-Mediterraneo sui Cambiamenti Climatici (CMCC), Bologna, Italy)

22 Simona Masina (CMCC; Istituto Nazionale di Geofisica e Vulcanologia (INGV), Bologna,
23 Italy)

24 Armin Köhl (Universität Hamburg (U-Hamburg), Hamburg, Germany)

25 Yonghong Yin, Li Shi, and Oscar Alves (Centre for Australian Weather and Climate Research,
26 Bureau of Meteorology (BOM), Melbourne, Australia)
27 Gregory Smith (Environment Canada, Québec, Canada)
28 You-Soon Chang (Geophysical Fluid Dynamics Laboratory, National Oceanic and Atmospheric
29 Administration (GFDL/NOAA), Princeton, New Jersey, USA; Kongju National University,
30 Kongju, South Korea)
31 Guillaume Vernieres (Science System and Applications, Inc., Lanham, Maryland, USA; Global
32 Modeling and Assimilation Office, National Aeronautics and Space Administration Goddard
33 Space Flight Center (GSFC/NASA/GMAO), Greenbelt, Maryland, USA)
34 Xiaochun Wang (Joint Institute for Regional Earth System Science and Engineering, University
35 of California, Los Angeles, California, USA)
36 Gael Forget, and Patrick Heimbach (Department of Earth, Atmospheric and Planetary Sciences,
37 Massachusetts Institute of Technology (MIT), Cambridge, Massachusetts, USA)
38 Ou Wang, Ichiro Fukumori, and Tong Lee (Jet Propulsion Laboratory (JPL), California Institute
39 of Technology, Pasadena, California, USA)
40 Hao Zuo, and Magdalena Balmaseda (European Centre for Medium-Range Weather Forecasts
41 (ECMWF), Reading, UK)

42

43 **Corresponding author**

44 Takahiro Toyoda, Oceanography and Geochemistry Research Department, Meteorological
45 Research Institute, Japan Meteorological Agency, 1-1 Nagamine, Tsukuba, 305-0052, Japan
46 E-mail: ttoyoda@mri-jma.go.jp

47

48

49 **Abstract**

50

51 The interannual-decadal variability of the wintertime mixed layer depths (MLDs) over the North
52 Pacific is investigated from an empirical orthogonal function (EOF) analysis of an ensemble of
53 global ocean reanalyses. The first leading EOF mode represents the interannual MLD anomalies
54 centered in the eastern part of the central mode water formation region in phase opposition with
55 those in the eastern subtropics and the central Alaskan Gyre. This first EOF mode is highly
56 correlated with the Pacific decadal oscillation index on both the interannual and decadal time
57 scales. The second leading EOF mode represents the MLD variability in the subtropical mode
58 water (STMW) formation region and has a good correlation with the wintertime West Pacific
59 (WP) index with time lag of 3 years, suggesting the importance of the oceanic dynamical
60 response to the change in the surface wind field associated with the meridional shifts of the
61 Aleutian Low. The above MLD variabilities are in basic agreement with previous observational
62 and modeling findings. Moreover the reanalysis ensemble provides uncertainty estimates. The
63 interannual MLD anomalies in the first and second EOF modes are consistently represented by
64 the individual reanalyses and the amplitudes of the variabilities generally exceed the ensemble
65 spread of the reanalyses. Besides, the resulting MLD variability indices, spanning the 1948-
66 2012 period, should be helpful for characterizing the North Pacific climate variability. In
67 particular, a 6-year oscillation including the WP teleconnection pattern in the atmosphere and
68 the oceanic MLD variability in the STMW formation region is first detected.

69

70

71 **Keywords**

72 ocean reanalysis, mixed layer depth, North Pacific, mode water, Pacific decadal oscillation,
73 West Pacific teleconnection pattern

74

75

76 **1 Introduction**

77

78 Most of the properties of the water masses in the global ocean are determined by the air-sea
79 interaction and turbulent mixing within the surface mixed layer (ML) and by subduction down to
80 the ventilated thermocline layer (Pedlosky 1996). The ML processes, hence, characterize the heat
81 and freshwater cycle in the upper ocean and are also an important component of the bio-
82 geochemical cycle (e.g., Takahashi 1997). Since the amount of subduction from the ML is largely
83 dependent upon the spatial distribution of the mixed layer depth (MLD) (e.g., via lateral induction;
84 Huang and Qiu 1994), the water-mass variability is strongly affected by the spatio-temporal MLD
85 variability. Accurate description of the latter is therefore required for better understanding and
86 characterizing the climate variability.

87

88 Previous studies have described the observed features of global MLD distribution based on the
89 climatological temperature and salinity (TS) data (e.g., Levitus 1982; Monterey and Levitus 1997;
90 Kara et al. 2003). de Boyer Montegut (2004) estimated the monthly variation in the global MLD
91 distribution by processing individual profiles of the TS observations. These studies have clarified
92 global features in the seasonal cycle of MLD climatology. Recently, observations by the Argo
93 hydrographic array have facilitated the description of the interannually-varying global MLD
94 distribution (e.g., Hosoda et al. 2010). However, the spatial resolution and temporal coverage of
95 the Argo data are still limited, particularly since decent coverage is practically limited to the last

96 century, which restricts applications to time scales of less than a decade.

97

98 The interannual-decadal variability of the MLDs in the water-mass formation regions has been
99 investigated in association with the analysis of water masses, such as mode waters (e.g., Hanawa
100 and Talley 2001; Speer and Forget 2013), by both observational and modeling studies (e.g., Peng
101 et al. 2006; Joyce et al. 2009). In the North Pacific, the most prominent interannual-decadal
102 variability is known to be the Pacific decadal oscillation (PDO; Kawasaki 1991), which is often
103 characterized by the "PDO index" as defined by the leading principal component of the North
104 Pacific sea surface temperature (SST) variability poleward of 20°N (Mantua et al. 1997). A
105 stronger (weaker) Aleutian Low along with stronger (weaker) westerlies and lower (higher) SSTs
106 in the western-central North Pacific is represented by a positive (negative) PDO index. Several
107 studies have explored the MLD variation in the formation region of the central mode water
108 (CMW; $\sim 26.2\sigma_\theta$, 9-12°C; Suga et al. 1997) in response to the PDO, particularly the decadal (or
109 interdecadal) regime shifts associated with the PDO (such as in 1976-1977) (e.g., Deser et al.
110 1996; Yasuda and Hanawa 1997; Schneider et al. 1999; Yasuda et al. 2000; Ladd and Thompson
111 2002; Qu and Chen 2009).

112

113 In addition to the aforementioned MLD variability in the CMW formation region, recent studies
114 (e.g., Qiu and Chen 2006; Qiu et al. 2007; Oka 2009) have investigated another important MLD
115 variability in the Kuroshio recirculation gyre region, where the subtropical mode water (STMW;
116 $\sim 25.2\sigma_\theta$, 15-19°C; Masuzawa 1969) is formed. They showed that the sea surface height and main
117 thermocline depth anomalies generated by the wind stress curl anomalies in the central subtropics
118 propagate westward and then influence the Kuroshio recirculation gyre region, leading to the
119 changes in the wintertime MLD and STMW thickness with time lag of a few years (e.g., Qiu and

120 Chen 2005). In these studies, the wind stress curl variability in the central subtropics is mainly
121 attributed to the Aleutian Low activity and hence can be related to the PDO index (e.g., Oka and
122 Qiu 2012) or to similar indices related with variations in the intensity of the Aleutian Low (e.g.,
123 North Pacific index (NPI; Trenberth and Hurrell 1994)). On the other hand, Sugimoto and Hanawa
124 (2010) proposed that the meridional shifts of the Aleutian Low are more important in explaining
125 the variability in the Kuroshio recirculation gyre region than the change in intensity of the
126 Aleutian Low represented by the PDO index. Meridional shifts of the Aleutian Low are related to
127 the West Pacific (WP) teleconnection pattern (Wallace and Gutzler 1981) and do not correlate
128 significantly with the intensity variation (Sugimoto and Hanawa 2009). Therefore, conflicting
129 causes have been suggested for the MLD variability in the Kuroshio recirculation gyre region
130 based on relatively short-term observation analyses: one group pointed out the dominant role of
131 the change in intensity of the Aleutian Low, and another group suggested the influence of the
132 meridional movement of the Aleutian Low. These should be investigated based on reliable long-
133 term products.

134

135 Subject to the El Niño-Southern Oscillation, the PDO pattern exhibits the interannual modulation
136 (e.g., Newman et al. 2003). The accurate description of the interannual-decadal MLD variability
137 on the basin scale is thus required for further understanding and characterizing the water-mass
138 variability in relation to the climate variability in the North Pacific (e.g., PDO). Although the
139 interannual variability of the MLDs on the basin scale has recently been investigated using the
140 Argo float data (e.g., Oka et al. 2007), this is arguably a very short period. Therefore, it is of value
141 to identify the long-term basin-scale MLD variability by fully utilizing observational datasets
142 available and our knowledge of the ocean dynamics (e.g., ocean models).

143

144 Ocean syntheses use the output of dynamical models combined with observations using statistical
145 technique and hence can provide MLDs at every defined grid point and time step, although they
146 are inevitably influenced by errors in the dynamical models, observations and assimilation
147 methods. Due to the recent increase in a variety of observations and in response to advances in
148 modeling and assimilation techniques, ocean syntheses have been improved to the level for
149 practical use (e.g., Lee et al. 2009). For example, Toyoda et al. (2011) analyzed the relative
150 contributions of the 3 dominant physical processes to the interannual variability of the North
151 Pacific eastern subtropical mode water (ESTMW; $24.0-25.4\sigma_{\theta}$, $16-22^{\circ}\text{C}$; Hautala and Roemmich
152 1998) formation due to the wintertime ML deepening, by using an ocean state estimation product
153 obtained by a 4 dimensional variational data assimilation experiment for the 1990s. This analysis
154 should be revisited for the more recent period using the Argo float data, especially since the
155 salinity observations are needed for the reproduction of the ML properties (Oka and Qiu 2012).
156 In addition, new ocean synthesis products have continuously been generated by different
157 institutions. Therefore, it is appropriate to revise the MLD estimates using the last generation of
158 ocean synthesis products.

159

160 To promote the increased use of ocean syntheses, the Global Synthesis and Observations Panel
161 (GSOP) of the Climate Variability and Predictability (CLIVAR) has recently initiated the Ocean
162 Reanalyses Intercomparison Project (ORA-IP), whose major goal is the inter-evaluation of global
163 ocean syntheses produced in the operational and research centers from various aspects (MLD,
164 heat and salt content, steric height, sea level, surface heat fluxes, depth of the 20 degree isotherm
165 and sea ice; Balmaseda et al. 2015). As part of this project work, Toyoda et al. (2015) have
166 investigated the fidelity in MLD of a suit of global ocean estimates consisting of two model-
167 independent estimates, produced by using only observations and 17 ocean syntheses, produced

168 using data assimilation approaches that combine ocean models and observations based on the
169 maximum likelihood principle ("reanalyses" hereafter). In addition to the discussion on biases in
170 the MLDs of the individual syntheses, they demonstrated that the skillful MLD reproduction for
171 both the seasonal cycle and interannual variability is possible by using the ensemble mean of the
172 reanalyses. They discussed that ocean reanalyses effectively synthesize oceanic and atmospheric
173 (via surface forcing from atmospheric reanalyses) observations and the dynamical models, with
174 their model errors cancelling out through ensemble averaging, suggesting great potential for better
175 analyzing the upper ocean processes.

176

177 In this study, we focus on the interannual-decadal variability of the wintertime MLDs in the North
178 Pacific represented in the ensemble mean of the reanalyses. The ensemble mean MLD field along
179 with information on its uncertainty derived from the ensemble spread allows a more quantitative
180 investigation than previous analyses (e.g., Toyoda et al. 2011). The aforementioned study (Toyoda
181 et al. 2015) focused on the validation of MLDs from ocean reanalyses using the Argo float data
182 (e.g., Hosoda et al. 2010). The current study, however, is not limited to the Argo era, but covers
183 the full temporal record of the reanalyses, which allows analyzing the relationship between the
184 MLD variability in the North Pacific and the interannual-decadal scale climate variability. Section
185 2 describes the ensemble mean MLD field derived from the reanalyses as well as other datasets
186 used in this study. The North Pacific MLD variability on an interannual-decadal time scale is
187 investigated in section 3. The summary and discussion are given in section 4.

188

189

190 **2 Data**

191

192 Monthly MLD fields estimated from 2 observation-only analyses and 17 reanalyses (Table 1) are
193 provided by the operational and research centers as an ORA-IP activity. These
194 syntheses/reanalyses are all different in ocean general circulation model, resolution, surface
195 forcing, ML parameterization, assimilated data and assimilation method (see details in Toyoda et
196 al. 2015). MLDs are obtained from the monthly mean TS fields on the original grids for the
197 individual datasets and then interpolated onto the common longitude-latitude grids at one-degree
198 intervals.

199

200 In the present study, we use a density criterion for the MLD definition (e.g., Levitus 1982), i.e.,
201 MLD is defined as the depth where potential density exceeds the 10-m depth value by 0.125 kg m^{-3} .
202 Toyoda et al. (2015) revealed that this definition results in an MLD field with less errors
203 relative to definitions using other criteria for potential density (0.03 kg m^{-3}) or potential
204 temperature (0.2°C and 0.5°C) in terms of both the seasonal cycle and interannual variability
205 since errors due to monthly averaging of profiles and to weak thermal stratification at high
206 latitudes are relatively small with this definition. Moreover, we use only wintertime maximum
207 MLDs, since we consider that such MLDs are thought to be a most important factor for the
208 thermocline layer dynamics via water mass formation and subduction. Note that the interannual
209 variability in MLD is generally dominated by the interannual variability of the wintertime MLDs
210 (except for the tropics). We pick out a wintertime maximum MLD in each location, year and
211 dataset from January-April (July-October) in the Northern (Southern) Hemisphere. These months
212 are chosen on the basis of the histogram for occurrence of the annual maxima of all the synthesis
213 MLDs (Fig. 1a). Although months when maximum MLDs occur can differ in each location within
214 the North Pacific (Fig. 1b), our approach allows the integrated analysis of the important MLD
215 features in the whole basin. Climatologies are defined for the wintertime maximum MLDs during

216 the 2001-2011 period (or longest available during this period). Hence, the month for producing
217 the climatology can vary among years at each grid point. Interannual anomalies from their
218 respective climatology are calculated for the individual products. Ensemble mean of the
219 climatology and interannual anomalies are then obtained from this ensemble of climatologies and
220 interannual anomalies (not including the observation-only analyses). Ensemble mean time series
221 (for the 1948-2012 period) are constructed by using these climatology and interannual anomaly
222 fields (referred to as "ENSMEAN" hereafter). Therefore, the number of reanalysis products
223 entering the ensemble mean time series varies with time, since the reanalyses products span
224 different time periods.

225

226 Monthly time series of the PDO index for the 1900-2014 period are obtained from the website of
227 the Joint Institute for the Study of the Atmosphere and Ocean, University of Washington
228 (<http://jisao.washington.edu/pdo/PDO.latest>). We calculate the year-to-year wintertime PDO time
229 series by averaging the monthly data from December of the preceding year to February of the
230 target year. We also use the annual PDO time series defined as the average from July of the
231 preceding year to June of the target year (with its center in winter) in order to compare with the
232 above wintertime time series.

233

234 Monthly time series of the WP index are obtained from the website of the National Weather
235 Service Climate Prediction Center, National Ocean Atmosphere Administration
236 (<http://www.cpc.ncep.noaa.gov/data/teledoc/wp.shtml>). Wintertime and annual WP time series
237 are calculated in the same manner as the PDO time series.

238

239 In addition, we use the JMA's historical observational data along the 137°E line in the North

240 Pacific in order to evaluate our results. Time series of temperatures in the STMW core in summer
241 at 137° E are obtained from the JMA website
242 (http://www.data.jma.go.jp/gmd/kaiyou/data/shindan/b_1/stmw/npstmw137e.txt). Observation
243 data of the geochemical parameters (nitrate concentration and apparent oxygen utilization (AOU))
244 are also obtained from the JMA website
245 (http://www.data.jma.go.jp/gmd/kaiyou/db/vessel_obs/data-report/html/ship/ship.php) and
246 interpolated onto the $25.2\sigma_{\theta}$ density surface through the Akima (1970) method after quality
247 control in the MRI. Annual mean values are calculated from the monthly time series averaged
248 over 28°N - 32°N .

249

250 We use the monthly values for sea level pressure (SLP) and latent and sensible heat fluxes from
251 both the JRA-55 (Kobayashi et al. 2015) and CORE (Large and Yeager 2004) datasets. The
252 COBE-SST (Ishii et al. 2005) dataset is also used.

253

254

255 **3. Result and discussion**

256

257 **3.1. Features of the ensemble mean field**

258

259 In this section, we explore the variability of the wintertime maximum MLDs in the North Pacific,
260 by taking advantage of the ensemble mean of the reanalysis MLDs (ENSMEAN). In doing so, we
261 first investigate the fidelity of ENSMEAN using metrics for evaluating our ensemble approach,
262 which are based on the ensemble spread and the correlation analysis.

263

264 Figure 2 shows the spatial distributions of the reanalysis ensemble mean and spread of the
265 wintertime maximum MLDs for the 2001-2011 period. Ensemble spread is defined here as the
266 standard deviation of the departure of each reanalysis from the ensemble mean at each grid point
267 and each year (e.g., Xue et al. 2012), which gives a measure of the uncertainty in the ensemble
268 mean. The ensemble spread distribution for the absolute wintertime maximum MLDs (Fig. 2b)
269 shows relatively large values in regions of large ensemble mean MLDs (Fig. 2a) such as in the
270 subarctic North Atlantic. A similar relation can be seen between the ensemble spread (Fig. 2d)
271 and the standard deviation of the ensemble mean (Fig. 2c) for the interannual anomalies (see
272 definition in Section 2). In addition, large values for the ensemble spread can be seen in the polar
273 regions, where large estimation errors of MLD were reported to arise primarily from the poor
274 potential of both model and assimilation experiments in representing the physical processes there
275 (e.g., deep convection and sea ice processes; see Toyoda et al. 2015). In the North Pacific, the
276 ensemble spread values for the absolute MLDs are mostly smaller than 60 m in the Kuroshio
277 Extension region and the Bering and Okhotsk Seas, where the ensemble mean MLDs are larger
278 than 150 m. On the other hand, the ensemble spread values are generally smaller than 20 m in
279 other regions of smaller MLDs. Note that the large values located in the northern part of the Japan
280 Sea are caused by the differences in both the amplitude and location between the reanalyses in
281 association with the small-scale deep convections off the Vladivostok (e.g., Senjyu and Sudo
282 1994). For the interannual anomalies, the ensemble spread values are even smaller: 30-40 m in
283 the Kuroshio Extension region and less than 10 m in most of the other open seas (Fig. 2d). These
284 values, in particular for the interannual anomalies, will be compared with the amplitude of the
285 analyzed variability in the following subsections. Note that, since the signal (standard deviation
286 of the ensemble mean anomalies) to noise (spread around the ensemble mean anomalies) ratio is
287 generally near 1 (Fig. 2e), the signal may not be well resolved.

288

289 The ensemble spread provides important information on the uncertainty of the ensemble mean
290 field based on root mean square differences. However, it gives no information about whether
291 ensemble members are exhibiting the same variability, i.e., the sign of the anomaly cannot be
292 properly evaluated by this metric. This is particularly in the present case that the amplitudes of
293 the variations in the individual reanalyses may differ depending on their configurations (e.g.,
294 mixed layer models). A better indicator of coordinated behavior would be the correlation between
295 the ensemble members and ensemble mean. In this study, we will use the averaged correlation of
296 all ensemble members with the ensemble mean as a qualitative indicator of a coordinated response
297 among the ensemble members.

298

299 Figure 3 exhibits the averaged correlation coefficients for the interannual anomalies between
300 ENSMEAN and the individual reanalyses. These values indicate the degree of consistency in
301 representing the interannual anomalies by the individual products. Hence, in addition to the
302 ensemble spread, the above values can be used for assessing the fidelity of the interannual
303 anomaly field of ENSMEAN. In this study, we underline the consistency in the signs of the
304 interannual anomalies. Therefore, we use the ENSMEAN MLDs only in those regions where the
305 averaged correlation coefficients between ENSMEAN and the individual reanalyses exceed the
306 90% confidence level (0.521). Although the regions with relatively large ensemble spread values
307 (e.g., in the Bering, Okhotsk and Japan Seas) are mostly eliminated by this procedure, we further
308 direct our attention to the open ocean region of the North Pacific (as indicated by the purple line
309 in Fig. 3) in the following analysis, in order to eliminate grid-scale un-eliminated data in the
310 marginal seas (the Okhotsk, Japan and East China Seas).

311

312 Before the analysis of the wintertime maximum MLDs of ENSMEAN, we compare those between
313 ENSMEAN and the observation-only analyses (EN3v2a and ARMOR3D). Figure 4 shows the
314 correlation coefficients among the 3 datasets. The correlations between EN3v2a/ARMOR3D and
315 ENSMEAN are generally greater than the correlation between the observation-only products in
316 most of the open ocean region. The comparison of the zonal mean values implies that this feature
317 is pronounced at low- and mid-latitudes (Fig. 4d). This is in contrast to the averaged correlation
318 between the observation-only analyses and the individual reanalyses (dashed lines) which is lower
319 than the correlation between the observation-only analyses. These results for the wintertime
320 maximum MLDs are similar to the previous results for the whole monthly MLDs (Toyoda et al.
321 2015) and suggest a skillful reproduction of the interannual anomaly field for the wintertime
322 maximum MLDs thanks to the ensemble averaging approach using the reanalysis estimates.

323

324 **3.2 Variability in the central subtropical North Pacific**

325

326 We perform an empirical orthogonal function (EOF) analysis for the interannual anomalies of the
327 wintertime maximum MLDs of ENSMEAN in the open ocean region of the North Pacific (within
328 the region bounded by the purple line in Fig. 3), and with the consistency of the ensemble
329 members at the 90% confidence level (correlation coefficients above 0.521 – the orange/red
330 regions in Fig. 3; thus, the Bering Sea is partly included, but only the small portions that exceed
331 the required consistency level) for the 2001-2011 period. This period is chosen because it is
332 common to most of the reanalyses (Table 1) and the Argo data are available for assimilation
333 throughout, although the full deployment of the Argo array was achieved by around 2004. Figure
334 5 shows the patterns and intensities of the first and second leading EOF modes for the 2001-2011
335 period (“EOF-1” and “EOF-2” hereafter), which explain 41% and 20% of the interannual

336 anomalies, respectively. Higher modes exhibit variations on much smaller scales and explain the
337 variance of less than 8% and will not be discussed any further in this study. Note that, in Fig. 5b,
338 d, projected time series of the EOF patterns are plotted for the other period of the EOF analysis
339 (before 2000 and for 2012; thin red lines).

340

341 For estimation of the influence of the selected period on the analysis, we perform another EOF
342 analysis for the same ENSMEAN interannual anomalies in the open ocean region of the North
343 Pacific for the whole 1948-2012 period. The first two EOF spatial patterns (Fig. 5a, c) and
344 principal components (PCs; “PC-1” and “PC-2” hereafter) (Fig. 5b, d) are basically similar to
345 those from the EOF analysis for the 1948-2012 period (e.g., red and blue lines for the PCs of the
346 2001-2011 and 1948-2012 EOF analyses, respectively), although the EOF spatial patterns for the
347 2001-2011 period show relatively confined structures with greater peak values (not shown). We
348 also compute the PC time series by projecting anomalies with respect to the 1948-2012 period
349 onto the EOF pattern based on the 2001-2011 period as discussed by Wen et al. (2014). The
350 resulting time series are further similar to the PCs from the EOF analysis for the 2001-2011 period.
351 This lends support to our expectation that the influence of the selected period to our below results
352 is negligible.

353

354 The EOF-1 pattern shows positive values in the western-central North Pacific while negative
355 values in the surrounding region (Fig. 5a). This pattern is similar to the SST distribution of the
356 PDO: negative (positive) SST anomalies of the PDO index correspond to positive (negative) MLD
357 anomalies of the EOF-1, consistent with previous studies (e.g., Ladd and Thompson 2002). Figure
358 6a indicates that the PC-1 (red line) actually correlates quite well with the wintertime PDO time
359 series (blue line), not only during the 2001-2011 period where the correlation coefficient is 0.77,

360 significantly non-zero at the 99% confidence level, but over the past 53 years (1948-2000) where
361 the correlation coefficient is 0.58 representing an even higher confidence level by virtue of the
362 larger temporal sample size. These results indicate that the MLD variability in this region is by
363 and large reproduced by ENSMEAN with a certain quality during the whole data period. Note
364 that the wintertime (December-February) time series are used here since the atmosphere-ocean
365 interaction is strong in this season (e.g., Trenberth and Hurrell 1994).

366

367 In the EOF-1 pattern (Fig. 5a), large positive values up to 30-40 m can be seen in the central
368 subtropics. This region corresponds to the eastern part of the CMW formation region. The typical
369 amplitude of this variability (Fig. 2c) averaged over this region (180° - 160° W, 32° N- 42° N; purple
370 box in Fig. 5a) is 30 m, while the ensemble spread of the interannual anomalies for ENSMEAN
371 (Fig. 2d) averaged over this region is 26 m. This suggests that the analyzed variability is generally
372 reliable when the amplitudes of the PC-1 are greater than the ratio of these values (0.87; Fig. 2e)
373 approximately. Moreover, the averaged correlation for the interannual anomalies between
374 ENSMEAN and the individual reanalyses is significant at a 99% confidence level in this region
375 (Fig. 3), i.e., the EOF-1 variability in this region is realized in most of the reanalyses at least in
376 terms of its sign. The ENSMEAN interannual MLD anomaly averaged over this region is very
377 coherent with the PC-1 (Fig. 6a) and also by and large vary with the interannual MLD anomalies
378 for the individual reanalyses as shown in Fig. 6b. These results support the idea that the rather
379 large ensemble spread seen in Fig. 2d is caused by the spread of the amplitude of the variation,
380 rather than on the sign of the MLD anomaly. It is also shown that the ensemble spread does not
381 change much during the whole 1948-2012 period. Therefore, the wintertime MLD variability in
382 this region generally maintains its correlation to the wintertime PDO index during the entire
383 period.

384

385 The above results introduce the variability on interannual time scales. Previous studies reported
386 the influence of the PDO on the decadal time scale. In our result, the MLD anomalies of
387 ENSMEAN averaged over the eastern part of the CMW formation region (green line in Fig. 6b)
388 is -17 m for the period before the regime shift associated with the PDO (1972-1976), which
389 increases to $+18$ m for the period after the regime shift (1977-81). This is in broad agreement to
390 previous observational and modelling studies focusing on the differences between the periods
391 before and after the 1976-1977 regime shift (e.g., Yasuda and Hanawa 1997; Ladd and Thompson
392 2002). Figure 6c shows the smoothed time series for the PC-1 and the wintertime PDO index via
393 a band-pass filter of 7-54 years based on the Fourier transform, which illustrates the presence of
394 a significant correlation between these time series on the decadal time scale (the correlation
395 coefficient is 0.74 for the 1955-2005 period), although the amplitude of the multi-decadal MLD
396 variability appears smaller than that of the multi-decadal PDO variability. Qu and Chen (2009)
397 investigated the MLD variability in relation to the variability of the annual subduction rate on the
398 decadal time scale in the North Pacific. They demonstrated that the time evolution of the
399 combined (MLD and subduction rate) variability correlates with the PDO index although they
400 also described that their results (especially for the first half of their simulation for 1950-2003)
401 could be influenced by both inaccurate forcing and inappropriate initial conditions of the model.
402 Our results using an ensemble of the reanalyses are in good agreement with these past studies.

403

404 **3.3 Variability in the eastern subtropical and subarctic regions**

405

406 The EOF-1 pattern (Fig. 5a) also shows interannual anomalies in the surrounding region with an
407 opposite sign to those in the western-central North Pacific. Three regions with relatively large

408 interannual anomalies are highlighted in this study: the ESTMW formation region (145°W-135°
409 W, 22°N-30°N, green square in Fig. 5a), the central Alaskan Gyre (160°W-140°W, 45°N-53°N,
410 orange square in Fig. 5a) and the Bering Sea (175°E-170°W, 53°N-60°N, red square in Fig. 5a).
411 The ensemble spread (Fig. 2d) averaged over each of these regions is 12 m, 7 m and 22 m,
412 respectively. The averaged correlations for the interannual anomalies between ENSMEAN and
413 the individual reanalyses are at a 95% confidence level in the ESTMW formation region and the
414 central Alaskan Gyre (Fig. 3). On the other hand, the correlation is low in the Bering Sea and
415 therefore not much data is used for the EOF analysis there (i.e., the data in the green-shaded area
416 in Fig. 3 are eliminated from the EOF analysis). Accordingly, we consider the MLD variability of
417 ENSMEAN in the Bering Sea to be not reliable, although the year of coldest wintertime SST,
418 1976 (2008) over the 1970-2008 period (after 2005), as reported in a previous study (Zhang et al.
419 2010) corresponds to the year of greatest wintertime MLD of ENSMEAN (not shown).

420

421 Figure 7 compares the PC-1 and the ENSMEAN interannual anomalies of the wintertime
422 maximum MLDs in the ESTMW formation region (Fig. 7a) and the central Alaskan Gyre (Fig.
423 7b). The MLD anomalies (green lines) in both regions generally show negative correlations with
424 the PC-1 (red lines) and thus with the wintertime PDO index (from Fig. 6) on both the interannual
425 and decadal time scales. The interannual MLD anomalies in the ESTMW formation region (Fig.
426 7a) are consistent with the previous study for the ESTMW variability during the 1991-2000 period
427 (Toyoda et al. 2011) but using an older version of the K7-ODA (ESTOC) reanalysis used in this
428 study (Table 1). In addition, the present results reveal that the ESTMW formation region is located
429 in the periphery of the PDO pattern with positive SST anomalies when the PDO index is positive.
430 This was not resolved in the SST patterns of the PDO as shown in previous studies (e.g., Mantua
431 et al. 1997) and thus has not been argued before.

432

433 Figure 7a exhibits that the negative correlation between the MLD anomalies and PC-1 on both
434 the interannual and decadal time scales generally holds during the entire time record. It is also
435 shown that the ensemble spread does not change much during the whole 1948-2012 period. These
436 facts support that ENSMEAN represents realistic features for both the interannual and decadal
437 variabilities in the ESTMW formation region. In contrast, over the central Alaskan Gyre (Fig. 7b)
438 the ensemble spread values are remarkably larger before 2000 than after 2001. This suggests that
439 in this region the data constraint during the assimilation is relatively weak without the Argo
440 observations. Note that the ensemble spread values become even smaller after 2004 possibly due
441 to the full deployment of the Argo array. The differences in phase between the smoothed time
442 series of the interannual MLD anomalies and PC-1, particularly before 1970, might reflect this
443 deficiency. Based on observations at Ocean Station Papa, Freeland and Cummins (2005)
444 demonstrated that the wintertime MLDs were shallower during El Niño events (1983, 1998 and
445 2003). Our result is qualitatively consistent with their findings. In addition, positive anomalies in
446 the late 1960s and early 1970s and negative anomalies from the middle of 1970s to the middle of
447 1980s are evident (Fig. 7b), similar to the observational reports (Fig. 10 of Freeland and Cummins
448 (2005); Fig. 4 of Li et al. (2005)). Moreover, Li et al. (2005) indicated that the annual maximum
449 MLDs appear in winter for the 1957-1976 period but in spring (April) for the 1977-1996 period
450 at several stations along the Line P (between the Station Papa and Vancouver Island) with
451 deepening of the spring ML taking place recently. In our result, the percentage of the April
452 occurrence of the annual maximum MLDs in the Alaskan Gyre increases, although the most
453 frequent month is still March (Fig. 7c). Such a change in the seasonal cycle of MLD should also
454 be important for the ecosystem and thus fisheries in this region. The physical mechanism remains
455 for future work.

456

457 **3.4 Variability in the STMW formation region**

458

459 The EOF-2 pattern is characterized by the prominent variability in the Kuroshio recirculation gyre
460 region (Fig. 5c), where the mean wintertime MLDs are large (Fig. 4a) associated with the STMW
461 formation. The ensemble spread of the interannual anomalies (Fig. 2d) averaged over this region
462 (140°E - 160°E , 28°N - 36°N , purple box in Fig. 5c) is 23 m and the averaged correlation for the
463 interannual anomalies between ENSMEAN and the individual reanalyses is significant at a 95%
464 confidence level (Fig. 3). As shown in Fig. 8a, the time series of the ENSMEAN MLD anomalies
465 averaged over this region and PC-2 show coherent evolution on both the interannual and decadal
466 time scales. In addition, the ensemble spread generally maintains similar values over the entire
467 period, although a consistent flattening is observed in the last decade. According to these results,
468 it can be considered that both the interannual and decadal variabilities in this region as reproduced
469 in ENSMEAN are generally robust and well captured by the EOF-2 during the whole 1948-2012
470 period.

471

472 Recent observational studies regarding the STMW and wintertime MLD variations in this region
473 have pointed out the interesting features: For example, shallower MLDs were seen in 1997-1999
474 from the analysis for 1993-2004 by Qiu and Chen (2006; their Fig. 4b). Sugimoto and Hanawa
475 (2010) showed that the STMWs were thinner in the late 1990s and thicker in the middle of 2000s
476 from data for 1993-2008. The MLD anomalies in ENSMEAN (Fig. 8a) are generally consistent
477 with these observational studies.

478

479 Comparison between the PC-2 and time series of the summertime core temperatures of the STMW

480 along the 137°E line conducted by the JMA (Fig. 8b) provides another validation for the
481 interannual anomalies. It can be confirmed that, when the PC-2 is significantly negative (e.g., in
482 winter 1998), the STMW temperature is relatively high (e.g., in summer 1999) with the time lag
483 of about 1.5 year, since the EOF-2 is estimated from winter MLDs. The lagged (the EOF-2 leading
484 by 1.5 year) correlation coefficient for the PC-2 and the STMW core temperature for the 1981-
485 2011 period (after removal of the background trend) is -0.46 , which is significant at a 99%
486 confidence level.

487

488 The above historical observations by the JMA include the geochemical parameters, which
489 provides a valuable source for the independent validation of our result. Figure 8c compares the
490 PC-2 and time series of nitrate concentration and AOU at the STMW density ($25.2\sigma_{\theta}$) between
491 28°N to 32°N along the 137°E line. These geochemical parameters are relatively large (small)
492 when the PC-2 is negative (positive) with the time lag of a few years. It can be considered that
493 the lower values initiated at the STMW formation in the surface ML are better maintained in the
494 thermocline layer when the influence of the surrounding water is relatively small due to the
495 relatively thick STMW. The consistent relationship between the PC-2 and geochemical
496 parameters seen after the late 1960s supports a robust reproduction of the MLD variability
497 associated with the STMW variability in our result.

498

499

500 **3.5 Attribution of the variability in the STMW formation region**

501

502 Previous studies investigated the responses of the STMW (and wintertime MLDs in its formation
503 region) to the Aleutian Low activity with the time lag of a few years. Qiu et al. (2007) indicated

504 that the state of the Kuroshio Extension jet varies in response to the PDO forcing with the time
505 lag of about 4 years. The former strongly influences the STMW thickness (Qiu and Chen 2006).
506 For example, thicker STMW with greater wintertime MLDs is formed when the Kuroshio
507 Extension jet is stable. On the other hand, Sugimoto and Hanawa (2010) indicated the important
508 role of the WP forcing in determining the main thermocline depth in the Kuroshio recirculation
509 gyre region (with the time lag of about 3 years), which affects the STMW thickness.

510

511 In this study, we investigate the relationship between the PC-2, which represents the wintertime
512 MLD variability in the STMW formation region, and the PDO/WP time series. While the EOF-1
513 structure and its intensity are discussed using the wintertime PDO index (as in Ladd and
514 Thompson (2002) for example), seasonal changes of the indices might need to be taken into
515 consideration in terms of the delayed response, although the north-south dipole SLP anomalies of
516 the WP pattern are stronger in winter (Barnston and Livezey 1987). In fact, the wintertime WP
517 index was underlined to explain the Aleutian Low variability in Sugimoto and Hanawa (2009),
518 whereas the wind stress curl field regressed to the WP index in respective months was used in
519 Sugimoto and Hanawa (2010). As for the PDO index, the wintertime and annual time series are
520 equivalent with the correlation coefficient of 0.90 for the 1951-2012 period, which is much higher
521 than that for the WP index (0.42). Hence we use the annual PDO time series and both the annual
522 and wintertime WP time series in this subsection.

523

524 The lagged relationship of the above time series is shown in Fig. 9, in which positive MLD
525 anomalies represented by the positive PC-2 values in 2003 and 2004 (red line) are suggested be
526 generated by the dynamical response to the Aleutian Low activity around 1998-1999 (positive
527 values of the PDO (Fig. 9a), annual WP (Fig. 9b) and wintertime WP (Fig. 9c) indices), via the

528 westward propagation of baroclinic Rossby waves (e.g., Qiu et al. 2007; Sugimoto and Hanawa
529 2010). Figure 10a shows the correlation coefficients among these time series for each time lag.
530 Significant correlation at a 99% confidence level is only obtained by the simultaneous correlation
531 between the PC-2 and wintertime WP index. We will discuss this relation later. Although the
532 relation that the PDO index leads the PC-2 by 1 or 2 years is visible in 2000s (Fig. 9a), significant
533 correlation for such a time lag range (e.g., between -5 and -1 year) is not obtained from our long-
534 term analysis (Fig. 10a). Further, no significant correlation between the PC-2 and
535 annual/wintertime WP index is found for the time range of a few years by which the PC-2 lags or
536 leads the WP index.

537

538 The time series as shown in Fig. 9 rather emphasize the year-to-year variations. In general, the
539 dynamical response of the ocean to atmospheric disturbances takes place on longer time scales.
540 Therefore, we examine in the following the relationship between low-pass filtered time series
541 (Fig. 10b-d). No significant positive correlation for the PC-2 lagging the PDO or annual WP
542 indices is found (Fig. 10b, c, respectively). In contrast, the PC-2 and wintertime WP index low-
543 pass filtered by windows between 3-6 years exhibit significant positive correlation with the time
544 lags between 2-4 years (Fig. 10d). In particular, the correlation coefficient for the 3-year lag and
545 5-year low-pass filtered is significant at a 99% confidence level. This time lag is consistent with
546 the result of Sugimoto and Hanawa (2010). Note that the annual WP plot (Fig. 10c) also shows
547 positive values in the same range but these are much smaller and not significant. Therefore, the
548 wintertime WP index is plausible to explain the PC-2 with the time lag of 3 years (as the
549 wintertime WP index leads the PC-2) from our analysis.

550

551 Figure 10d also indicates significant positive correlations with the time lag of 3 years as the PC-

552 2 leads the wintertime WP index. Since a 3-year delayed response of the atmosphere is unlikely,
553 this can be attributed to the oscillatory feature of the wintertime WP index of about 6 years, which
554 is generally visible in Fig. 9c. In between these positive values, significant negative values are
555 visible with zero time lag, as seen in the plot of the raw time series (Fig. 10a) as described above.
556 From this result, we can consider that negative (positive) WP pattern is generated when the PC-2
557 is positive (negative). Therefore, the wintertime SST anomalies associated with the EOF-2 likely
558 act to force the atmosphere to generate the wintertime WP teleconnection pattern with the opposite
559 sign of the PC-2 (and the previous WP peak about 3 years before). This in turn changes the wind
560 stress field in the central North Pacific, which eventually influences the STMW formation region
561 as the sign of the PC-2 reverses with the time lag of about 3 years. This chain of processes leads
562 to the PC-2 cycle of about 6 years as discussed above (Fig. 10d).

563

564 Figure 11 shows the spectrum analysis for the PC-2 and the wintertime WP index. The power
565 spectra based on the maximum entropy method indicate a clear peak at the period of 5-10 years
566 for each of the time series. This is consistent with the aforementioned cycle of about 6 years.
567 However, it is known that the spectrum analysis based on the maximum entropy method
568 sometimes gives a false peak. In order to validate the above spectral peaks, another spectrum
569 analysis based on the fast Fourier transform is also conducted. Note that the distribution from this
570 analysis is generally rather noisy. For both time series, relatively large values are also obtained at
571 the period of 5-10 years when based on the fast Fourier transform. Although the resolution of
572 these analyses might not be enough to determine a 6-year cycle, these analyses at least support
573 the periodicities of both the PC-2 and the wintertime WP index around this period.

574

575 Figure 12 shows the regressed patterns to the PC-2 of the SLP, SST and surface turbulent heat

576 flux (THF; sum of latent and sensible heat fluxes; positive upward) fields. The regressed SLP
577 pattern (Fig. 12a) is almost the same as the negative wintertime WP pattern (e.g., Fig. 5 of
578 Sugimoto and Hanawa (2009)), which supports the large negative correlation between the PC-2
579 and wintertime WP index with zero time lag (Fig. 10d). Over most of the North Pacific, the SST
580 and THF anomalies have opposite signs (Fig. 12b). For example, the positive anomalies of THF
581 release to the atmosphere correspond to the negative SST anomalies in the south of Japan.
582 However, in the eastern part of the Kuroshio Extension region (yellow box approximately), there
583 exists a region where the anomalies have the same sign (positive) allowing the SST to increase
584 the THF and force the atmosphere. Note that this result is only slightly dependent on the forcing
585 dataset, differing little when the CORE dataset is used instead of the JRA-55 dataset as in Fig. 12.
586

587 Qiu and Chen (2006) indicated that the STMWs are relatively thick (thin) and thus the wintertime
588 MLDs in the STMW formation region are relatively large (small) when the Kuroshio Extension
589 jet is relatively strong and stable (weak and unstable). Several studies confirmed their point (see
590 Oka and Qiu 2012). Since the PC-2 represents the wintertime MLD variability in this region, the
591 above indication means that the Kuroshio Extension jet is relatively strong and stable (weak and
592 unstable) when the PC-2 is positive (negative). The state of the Kuroshio Extension jet possibly
593 affects the SSTs in the eastern part of the Kuroshio Extension: relatively higher (lower) SSTs can
594 be induced by the strong (weak) advection of the warm water, which leads to the positive
595 (negative) THF anomalies in this region, and thereby works on the atmosphere to generate the
596 negative (positive) WP teleconnection pattern. In fact, the core of the low pressure anomalies are
597 located around 180° , 35°N - 40°N corresponding to a large positive SST anomaly region (Fig.
598 12b). Note that the PDO pattern also exhibits the large SST anomalies in this region although the
599 maxima of both SST and SLP are located to the east. Therefore difference in the SST distribution

600 between the EOF-1 (PDO index) and EOF-2 (wintertime WP index) might be important in forcing
601 the atmosphere. A full description of the process for the 6-year oscillation including the oceanic
602 EOF-2 and atmospheric WP patterns awaits future work.

603

604

605 **4 Conclusion**

606

607 We have performed an EOF analysis for the wintertime MLD anomalies in the North Pacific
608 derived from an ensemble of 17 global ocean reanalyses. To ensure the validity of the analysis,
609 we use only data in the region where the ensemble members consistently represent the MLD
610 variability, by taking account of the correlation between the individual reanalyses and ensemble
611 mean. The EOF-1 represents the MLD anomalies centered in the eastern part of the CMW
612 formation region in phase opposition with those in the ESTMW formation region and central
613 Alaskan Gyre and its PC highly correlates with the PDO index on both the interannual and
614 decadal time scales. The EOF-2 represents the MLD variability in the STMW formation region
615 and its PC correlates with the wintertime WP index with the time lag of about 3 years.

616

617 By using the global ocean reanalyses obtained through data assimilation approaches that
618 combine ocean models and observations, an integrated analysis of the important MLD features
619 in the whole North Pacific during the 1948-2012 period is provided in this study. In fact, the
620 MLD variabilities represented by the EOF modes are by and large consistent with previous
621 studies that mainly focused on their particular events or locations (e.g., the regime shift in 1976-
622 1977). In addition, the ensemble use of the reanalyses allows more quantitative discussion. The
623 robustness of the variabilities in the key regions for the water mass formation in the North

624 Pacific is generally confirmed by using information on the uncertainty of the ensemble mean,
625 which is measured by the ensemble spread of the reanalyses.

626

627 It is obvious that the historical observations are of fundamental importance, without which neither
628 evaluation of the analysis nor realistic constraint to the assimilative models is possible. On the
629 other hand, the present study shows the great potential of the ensemble reanalyses for
630 investigating the climate variability. For example, mechanism of the recent deepening of the
631 spring ML in the Alaskan Gyre (Li et al. 2005) as reproduced in the reanalysis ensemble mean
632 can be investigated utilizing variables other than MLD. To carry this out, however, further
633 validation studies for the reanalysis products from various aspects as attempted in the ORA-IP
634 (e.g., Storto et al. 2015; see Balmaseda et al. 2015) are required.

635

636 To this date, conflicting causes have been suggested for the MLD variability in the STMW
637 formation region. This study provides the answer to the long-standing debate based on the long-
638 term assimilation products, that is, the meridional movement of the Aleutian Low is responsible
639 for the MLD variability in the STMW formation region. Furthermore, an oscillation of about 6
640 years which includes the WP teleconnection pattern in the atmosphere and the oceanic MLD
641 variability in the STMW formation region is first detected in this study. It is demonstrated that
642 the wintertime SST anomalies in the eastern part of the Kuroshio Extension associated with the
643 EOF-2 force the WP pattern with the opposite sign of the PC-2. This WP pattern induces the
644 change in the surface wind stress field in the central North Pacific, which, via the oceanic
645 dynamical response, eventually reverses the sign of the PC-2 with the time lag of about 3 years,
646 leading to about 6 years for the cycle of this process. The SST anomalies in the eastern part of
647 the Kuroshio Extension are possibly attributed to the variation in the Kuroshio Extension jet,

648 since the latter was pointed out by previous studies to have a close relation to the wintertime
649 MLD variability in the Kuroshio recirculation gyre region and hence the EOF-2. Although a full
650 description of the process remains for future work, identifying the oscillation of about 6 years in
651 this study might be able to give a new insight to understand the North Pacific climate variability,
652 such as in relation to the influence of the El Niño-Southern Oscillation of about 4 years and the
653 PDO of about 10 years.

654

655

656 **Acknowledgements**

657

658 The ORA-IP activity is a joint contribution and effort from the GSOP of CLIVAR and the
659 GODAE OceanView. We thank three anonymous reviewers for their constructive comments.
660 This work was partly supported by the Research Program on Climate Change Adaptation
661 (RECCA) of the Ministry of Education, Culture, Sports, Science and Technology of the
662 Japanese government (MEXT), by the Data Integration and Analysis System (DIAS) of the
663 MEXT, by the joint UK DECC/Defra Met Office Hadley Centre Climate Programme
664 (GA01101), by the UK Public Weather Service Research Programme, and by the European
665 Commission funded projects MyOcean (FP7-SPACE-2007-1) and MyOcean2 (FP7-SPACE-
666 2011-1). During the preparation of this article, our co-author Nicolas Ferry passed away. He was
667 an active and supportive member of the ORA-IP and CLIVAR-GSOP activities.

668

669

670 **References**

671

- 672 Akima H (1970) A new method of interpolation and smooth curve fitting based on local
673 procedures. *J Assoc Comput Mach* 17:589-603
674
- 675 Balmaseda MA, Hernandez F, Storto A, Palmer MD, Alves O, Shi L, Smith GC, Toyoda T,
676 Valdivieso M, Barnier B, Behringer D, Boyer T, Chang YS, Chepurin GA, Ferry N, Forget G,
677 Fujii Y, Good S, Guinehut S, Haines K, Ishikawa Y, Keeley S, Köhl A, Lee T, Martin M, Masina
678 S, Masuda S, Meyssignac B, Mogensen K, Parent L, Peterson KA, Tang YM, Yin Y, Vernieres
679 G, Wang X, Waters J, Wedd R, Wang O, Xue Y, Chevallier M, Lemieux JF, Dupont F, Kuragano
680 T, Kamachi M, Awaji T, Caltabiano A, Wilmer-Becker K, Gaillard F (2015) The Ocean
681 Reanalyses Intercomparison Project (ORA-IP). *J Operational Oceanogr* 8:s80-s97.
682 doi:10.1080/1755876X.2015.1022329
683
- 684 Barnston AG, Livezey RE (1987) Classification, seasonality and persistence of low-frequency
685 atmospheric circulation patterns. *Mon Wea Rev* 115:1083-1126
686
- 687 de Boyer Montegut C, Madec G, Fischer AS, Lazar A, Iudicone D (2004) Mixed layer depth
688 over the global ocean: An examination of profile data and a profile-based climatology. *J*
689 *Geophys Res* 109:C12003. doi:10.1029/2004JC002378
690
- 691 Deser C, Alexander MA, Timlin MS (1996) Upper-ocean thermal variations in the North Pacific
692 during 1970-1991. *J Clim* 9:1840-1855
693
- 694 Freeland HJ, Cummins PF (2005) Argo: a new tool for environmental monitoring and
695 assessment of the world's oceans, an example from the NE Pacific. *Prog Oceanogr* 64:31-44.

696 doi:10.1016/j.pocean.2004.11.002
697
698 Hanawa K, Talley LD (2001) Mode waters. In: Siedler G, Church J, J. Gould J (eds) Ocean
699 Circulation and Climate. Academic Press, NewYork, pp 373-386
700
701 Hautala SL, Roemmich DH (1998) Subtropical mode water northeast Pacific Basin. J Geophys
702 Res 103:13055-13066
703
704 Hosoda S, Ohira T, Sato K, Suga T (2010) Improved description of global mixed-865 layer
705 depth using Argo profiling floats. J Oceanogr 66:773-787. doi:10.1007/s10872-866 010-0063-3
706
707 Huang RX, Qiu B (1994) Three-dimensional structure of the wind-driven circulation in the
708 subtropical North Pacific. J Phys Oceanogr 24:1608-1622
709
710 Ishii M, Shouji A, Sugimoto S, Matsumoto T. (2005) Objective analyses of sea-surface
711 temperature and marine meteorological variables for the 20th century using ICOADS and the
712 Kobe Collection. Int J Climatol 25: 865-879
713
714 Joyce TM, Thomas LN, Bahr F (2009) Wintertime observations of subtropical mode water
715 formation within the Gulf Stream. Geophys Res Lett 36:L02607. doi:10.1029/2008GL035918
716
717 Kara AB, Rochford PA, Hurlburt HE (2003) Mixed layer depth variability over the global
718 ocean. J Geophys Res 108:3079. doi:10.1029/2000JC000736
719

- 720 Kawasaki T (1991) Long-term variability in the pelagic fish populations. In: Kawasaki T,
721 Tanaka S, Toba Y, Taniguchi A. (eds) Long-Term Variability of Pelagic Fish Populations and
722 Their Environment. Pergamon Press, New York, USA
723
- 724 Kobayashi S, Ota Y, Harada Y, Ebita A, Moriya M, Onoda H, Onogi K, Kamahori M,
725 Kobayashi C, Endo H, Miyaoka K, Takahashi K. (2015) The JRA-55 Reanalysis: General
726 specifications and basic characteristics. J Meteor Soc Japan, in press. doi:20.2151/jmsj.2015-
727 0001.
728
- 729 Ladd C, Thompson LA (2002) Decadal Variability of North Pacific Central Mode Water. J Phys
730 Oceanogr 32:2870-2881
731
- 732 Large WG, Yeager SG (2004) Diurnal to decadal global forcing for ocean and sea-ice models:
733 the data sets and flux climatologies. Technical Note TN-460+STR, NCAR, Boulder, Colorado,
734 USA, 105 pp
735
- 736 Lee T, Awaji T, Balmaseda MA, Grenier E, Stammer D (2009) Ocean state estimation for
737 climate research. Oceanography 22:160-167. doi:10.5670/oceanog.2009.74
738
- 739 Levitus S (1982) Climatological atlas of the world ocean. NOAA/ERL GFDL, Princeton NJ
740 USA, 173 pp
741
- 742 Li M, Myers PG, Freeland H (2005) An examination of historical mixed layer depths along line
743 P in the Gulf of Alaska. Geophys Res Lett 32:L05613. doi:10.1029/2004GL021911

744

745 Mantua NJ, Hare SR, Zhang Y, Wallace JM, Francis RC (1997) A Pacific interdecadal climate
746 oscillation with impacts on salmon production. *B Am Meteorol Soc* 78:1069-1079

747

748 Masuzawa J (1969) Subtropical mode water. *Deep Sea Res* 16:463-472

749

750 Monterey G, Levitus S (1997) Seasonal Variability of Mixed Layer Depth for the World Ocean.

751 NOAA Atlas NESDIS 14. U.S. Government Printing Office, Washington DC USA

752

753 Newman M, Compo GP, Alexander MA (2003) ENSO-forced variability of the Pacific decadal
754 oscillation. *J Climate* 16:3853-3857

755

756 Oka E, Qiu B (2012) Progress of North Pacific mode water research in the past decade. *J*

757 *Oceanogr* 68:5-20. doi:10.1007/s10872-011-0032-5

758

759 Oka E, Talley LD, Suga T (2007) Temporal variability of winter mixed layer in the mid-to high-
760 latitude North Pacific. *J Oceanogr* 63:293-307.

761

762 Pedlosky J (1996) Ocean circulation theory. Springer Berlin Heidelberg, 456 pp.

763 doi:10.1007/987-3-662-03204-6

764

765 Peng G, Chassignet EP, Kwon YO, Riser SC (2006) Investigation of variability of the North

766 Atlantic Subtropical Mode Water using profiling float data and numerical model output. *Ocean*

767 *Model*, 13:65-85. doi:10.1016/j.ocemod.2005.07.001

768

769 Press WG, Teukolsky SA, Vetterling WT, Flannery BP (1992) Numerical Recipes in
770 FORTRAN: The Art of Scientific Computing Second Edition. Cambridge Univ Press,
771 Cambridge UK, 963 pp.

772

773 Qiu B, Chen S (2006) Decadal variability in the formation of the North Pacific Subtropical
774 Mode Water: Oceanic versus atmospheric control. *J Phys Oceanogr* 36:1365-1380

775

776 Qiu B, Chen S, Hacker P (2007) Effect of mesoscale eddies on subtropical mode water
777 variability from the Kuroshio Extension System Study (KESS). *J Phys Oceanogr* 37:982-1000.
778 doi:10.1175/JPO03097.1

779

780 Qu T, Chen J (2009) A North Pacific decadal variability in subduction rate. *Geophys Res*
781 *Lett* 36:L22602. doi:10.1029/2009GL040914

782

783 Schneider N, Miller AJ, Alexander MA, Deser C (1999) Subduction of decadal North Pacific
784 temperature anomalies: Observations and dynamics. *J Phys Oceanogr* 29:1056-1070

785

786 Senjyu T, Sudo H (1994) The upper portion of the Japan Sea proper water, its source and
787 circulation as deduced from isopycnal analysis. *J Oceanogr* 50:663–690

788

789 Speer K, Forget G (2013) Global distribution and formation of mode waters. In: Siedler G,
790 Griffies SM, Gould J, Church JA (eds) *Ocean Circulation and Climate: A 21st Century*
791 *Perspective*. Academic Press, New York, pp 211-226. doi:10.1016/B978-0-12-391851-2.00009-

792 X

793

794 Storto A, Masina S, Balmaseda M, Guinehut S, Xue Y, Szekely T, Fukumori I, Forget G, Chang

795 Y-S, Good SA, Köhl A, Vernieres G, Ferry N, Peterson KA, Behringer D, Ishii M, Masuda S,

796 Fujii Y, Toyoda T, Yin Y, Valdivieso M, Barnier B, Boyer T, Lee T, Gourrion J, Wang O,

797 Heimback P, Rosati A, Kovach R, Hernandez F, Martin MJ, Kamachi M, Kuragano T,

798 Mogensen K, Alves O, Haines K, Wang X (2015) Steric sea level variability (1993-2010) in an

799 ensemble of ocean reanalyses and objective analyses. *Clim Dyn* (in press). doi:10.1007/s00382-

800 015-2554-9

801

802 Suga T, Takei Y, Hanawa K (1997) Thermostat distribution in the North Pacific subtropical

803 gyre: The central mode water and the subtropical mode water. *J Phys Oceanogr* 27:140-152

804

805 Sugimoto S, Hanawa K (2009) Decadal and interdecadal variations of the Aleutian Low activity

806 and their relation to upper oceanic variations over the North Pacific. *J Meteor Soc Japan* 87:601-

807 619. doi:10.2151/jmsj.87.601

808

809 Sugimoto S, Hanawa K (2010) Impact of Aleutian Low activity on the STMW formation in the

810 Kuroshio recirculation gyre region. *Geophys Res Lett* 37:L03606. doi:10.1029/2009GL041795

811

812 Takahashi T, Feely RA, Weiss RF, Wanninkhof RH, Chipman DW, Sutherland SC, Takahashi

813 TT (1997) Global air-sea flux of CO₂: An estimate based on measurements of sea-air pCO₂

814 difference. *P Natl Acad Sci*, 94:8292-8299

815

- 816 Toyoda T, Awaji T, Masuda S, Sugiura N, Igarashi H, Mochizuki T, Ishikawa Y (2011)
817 Interannual variability of North Pacific eastern subtropical mode water formation in the 1990s
818 derived from a 4-dimensional variational ocean data assimilation experiment. *Dynam Atmos*
819 *Oceans* 51:1-25. doi:10.1016/j.dynatmoce.2010.09.001
820
- 821 Toyoda T, Fujii Y, Kuragano T, Kamachi M, Ishikawa Y, Masuda S, Sato K, Awaji T,
822 Hernandez F, Ferry N, Guinehut S, Martin M, Peterson KA, Good S, Valdivieso M, Haines K,
823 Storto A, Masina S, Köhl A, Zuo H, Balmaseda M, Yin Y, Shi L, Alves O, Smith G, Chang YS,
824 Vernieres G, Wang X, Forget G, Heimbach P, Wang O, Fukumori I, Lee T (2015)
825 Intercomparison and validation of the mixed layer depth fields of global ocean syntheses. *Clim*
826 *Dyn* (in press). doi:10.1007/s00382-015-2637-7
827
- 828 Trenberth KE, Hurrell JW (1994) Decadal atmosphere-ocean variations in the Pacific. *Clim Dyn*
829 9:303-319
830
- 831 Wallace JM, Gutzler DS (1981) Teleconnections in the geopotential height field during the
832 Northern Hemispheric winter. *Mon Wea Rev* 109:784-812
833
- 834 Yasuda T, Hanawa K (1997) Decadal changes in the mode waters in the midlatitude North
835 Pacific. *J Phys Oceanogr* 27:858-870
836
- 837 Yasuda I, Tozuka T, Noto M, Kouketsu S (2000) Heat balance and regime shifts of the mixed
838 layer in the Kuroshio Extension. *Prog Oceanogr* 47:257-278. doi:10.1016/S0079-
839 6611(00)00038-0

840

841 Wen C, Kumar A, Xue Y (2014) Factors contributing to uncertainty in Pacific Decadal Oscillation
842 index. *Geophys Res Lett* 41:7980-7986. doi:10.1002/2014GL061992

843

844 Xue Y, Balmaseda MA, Boyer T, Ferry N, Good S, Ishikawa I, Kumar A, Rienecker M, Rosati

845 AJ, Yin Y (2012) A comparative analysis of upper-ocean heat content variability from an
846 ensemble of operational ocean reanalyses. *J Clim* 25:6905-6929. doi:10.1175/JCLI-D-11-

847 00542.1

848

849 Zhang J, Woodgate R, Moritz R (2010) Sea ice response to atmospheric and oceanic forcing in
850 the Bering Sea. *J Phys Oceanogr* 40:1729-1747. doi:10.1175/2010JPO4323.1

851

852

853 **Tables**

854

855 **Table 1** Producing centers, contact parsons and duration of the syntheses used in this study

Synthesis	Center	Contact parson	Duration
<i>(Observation-only analysis)</i>			
EN3v2a	Met Office	S. Good	1993-2011
ARMOR3D	CLS	S. Guinehut	1993-2010
<i>(Reanalysis)</i>			
G2V3	Mercator Océan	F. Hernandez	1993-2011
C-GLORS	CMCC	A. Storto	1991-2011
UR025.4	U-Reading	M. Valdivieso	1993-2010
GloSea5	Met Office	M. Martin	1993-Jul. 2012
ORAS4	ECMWF	M. Balmaseda	1958-2011
ORAP5	ECMWF	H. Zuo	1993-2012
GECCO2	U-Hamburg	A. Köhl	1948-Nov. 2011

MERRA	GSFC/NASA/GMAO	G. Vernieres	1993-2011
ECCO-NRT	JPL/NASA	O. Wang	1993-2011
ECCO-v4	JPL/MIT/AER	X. Wang	1992-2010
ECDA	GFDL/NOAA	Y.-S. Chang	2005-2011
PEODAS	BoM	O. Alves	1980-2012
K7-ODA (ESTOC)	RCGC/JAMSTEC	S. Masuda	1975-2011
K7-CDA	CEIST/JAMSTEC	Y. Ishikawa	2000-2006
MOVE-G2	MRI/JMA	T. Toyoda	1993-2012
MOVE-CORE	MRI/JMA	Y. Fujii	1948-2007
MOVE-C	MRI/JMA	Y. Fujii	1950-2011

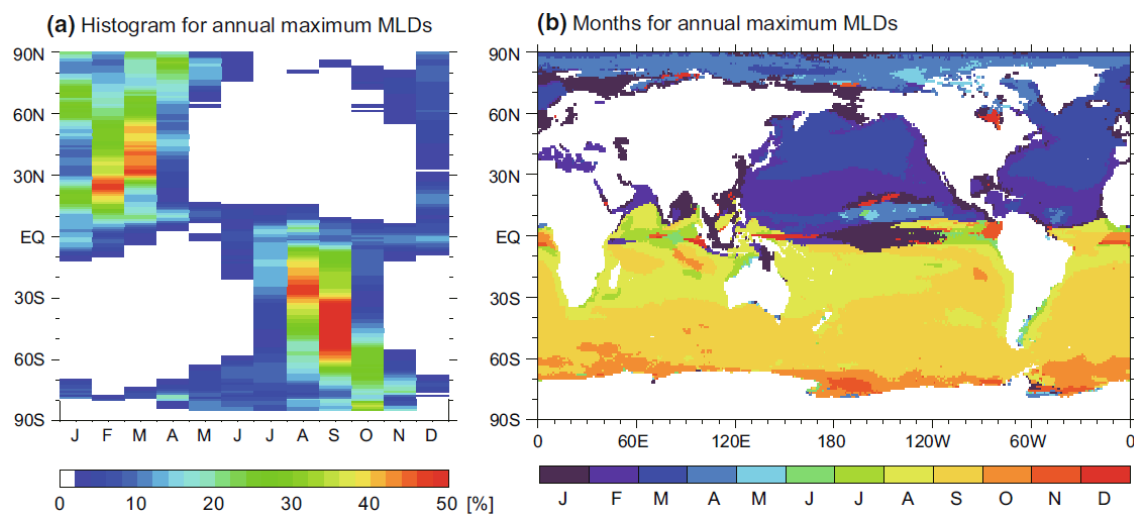
856 Durations submitted to the ORA-IP are sometimes shorter than those of the original syntheses

857

858

859 **Figures**

860



861

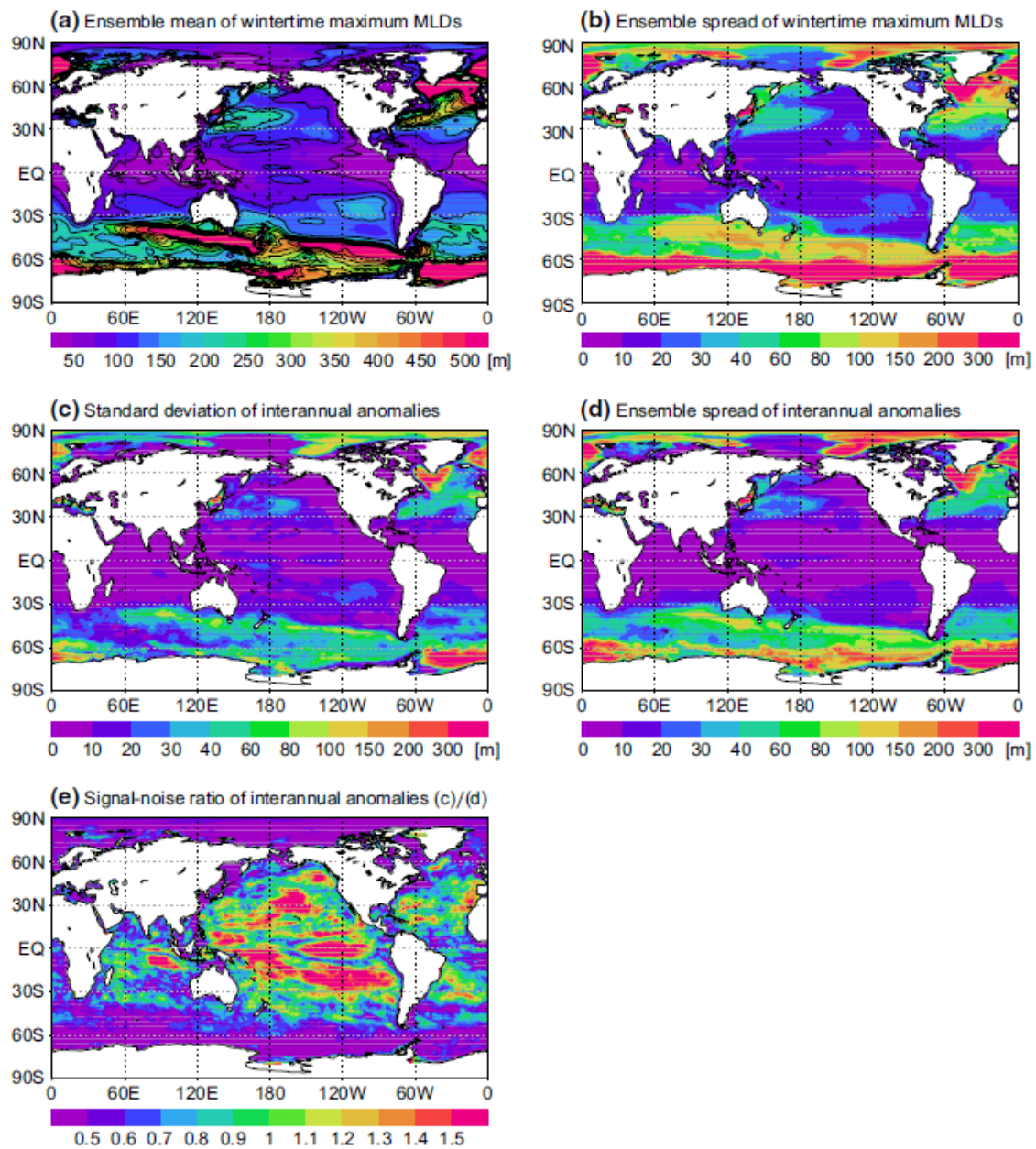
862 **Fig. 1** (a) Histogram for the occurrence of the annual maximum MLDs for each month and latitude

863 normalized by the zonal sum of the values (units in %). (b) Distribution of the months when the

864 annual maximum MLDs occur most frequently. The month of the annual maximum MLD

865 estimated for each grid point, year and synthesis is used for these plots.

866



867

868 **Fig. 2** Distributions of the ensemble mean (a) and spread (b) of the wintertime maximum MLDs,

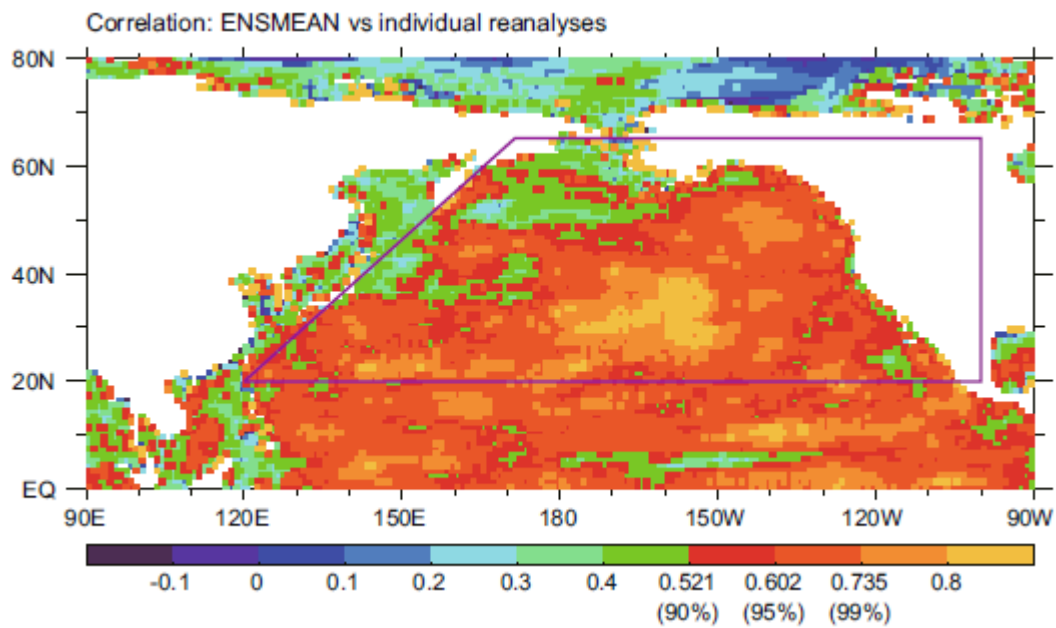
869 the standard deviation of the interannual anomalies of the ensemble mean wintertime maximum

870 MLDs (c), the ensemble spread of interannual anomalies of the wintertime maximum MLDs (d)

871 and signal to noise ratio of the interannual anomalies (e; defined here as (c) divided by (d)). Values

872 are estimated from all the 17 reanalyses and averaged over the 2001-2011 period.

873



874

875 **Fig. 3** Distribution of the averaged correlation coefficients of the wintertime maximum MLDs

876 between ENSMEAN and the individual 17 reanalyses for the 2001-2011 period. Note that the

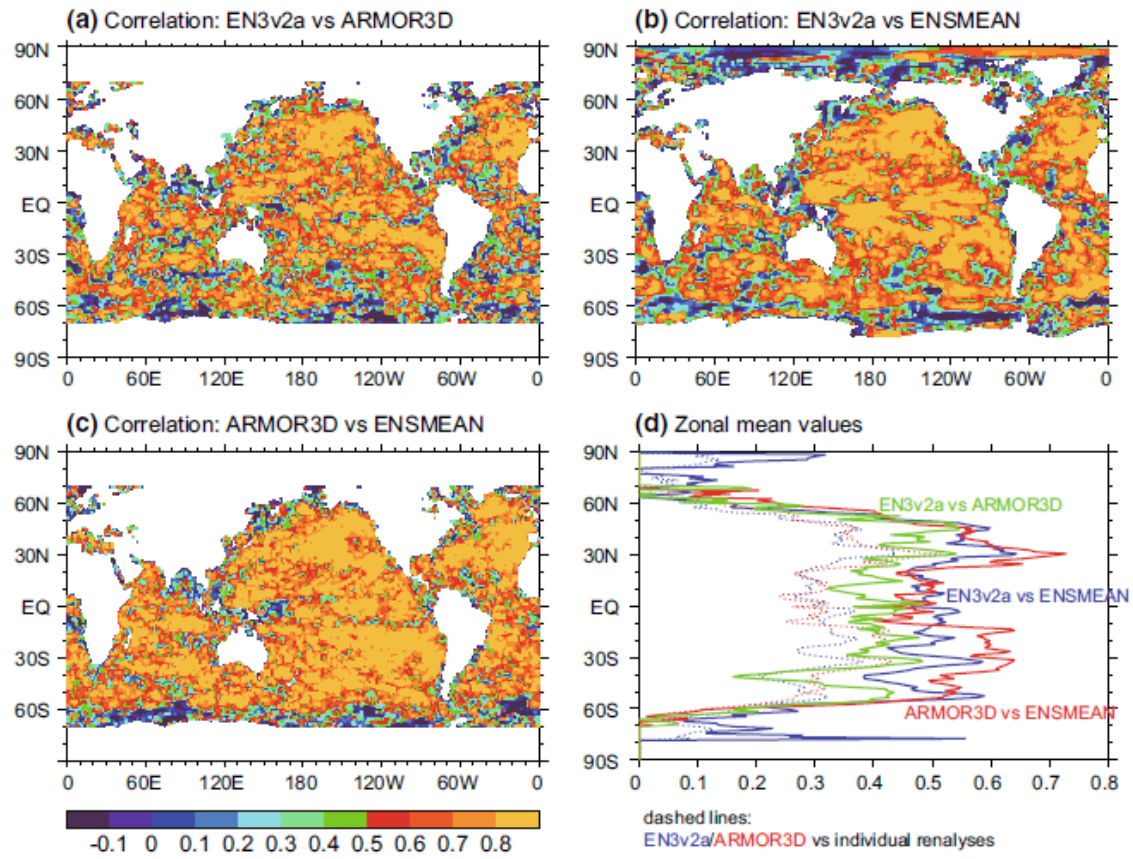
877 color bar differs from that in Fig. 4. Values at the confidence levels of 90, 95 and 99%

878 highlighted in this figure. Here, the sample size is the number of years, 11. The purple line

879 indicates the open ocean region of the North Pacific within which we use the data for the EOF

880 analysis (see text).

881



882

883 **Fig. 4** (a-c) Distributions of correlation coefficients of the wintertime maximum MLDs between

884 EN3v2a and ARMOR3D (a), between EN3v2a and ENSMEAN (b) and between ARMOR3D and

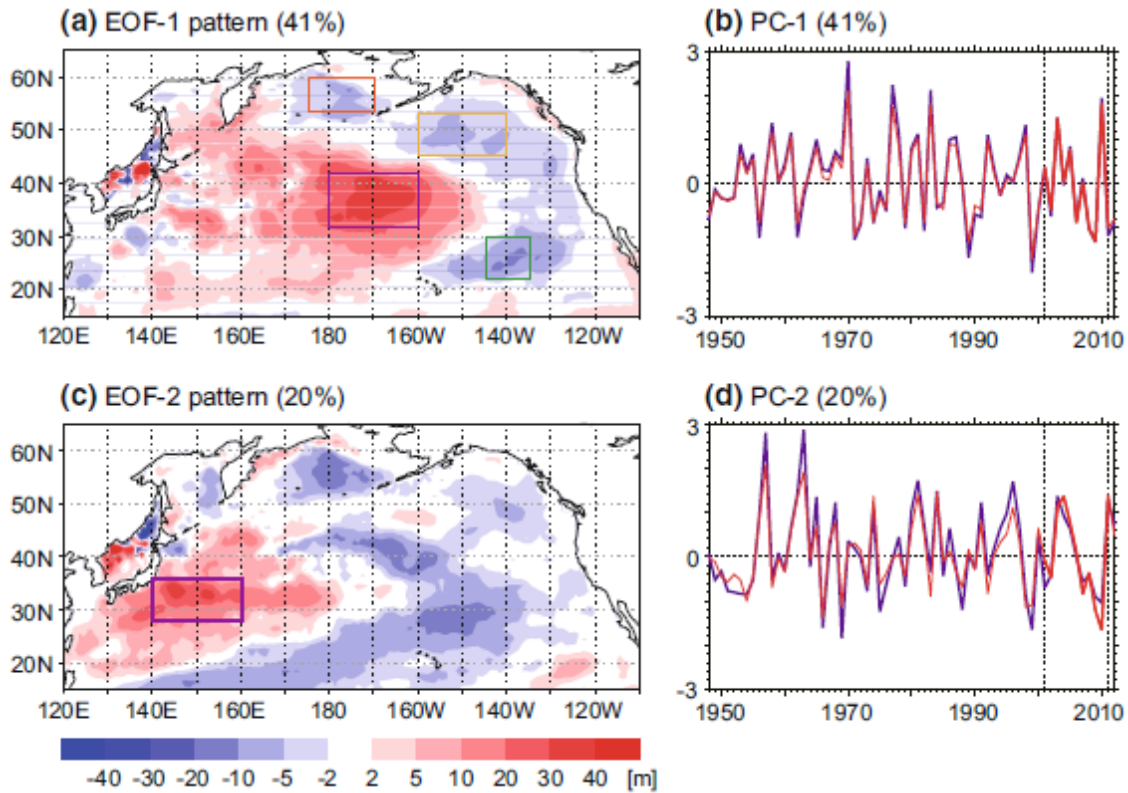
885 ENSMEAN (c). Note that the color bar differs from that in Fig. 3. (d) Zonal mean values for the

886 above distributions (a-c; solid lines) and the averaged correlation coefficients between

887 EN3v2a/ARMOR3D and the individual 17 reanalyses (dashed lines). Winter maximum MLDs

888 for the 2001-2011 period are used.

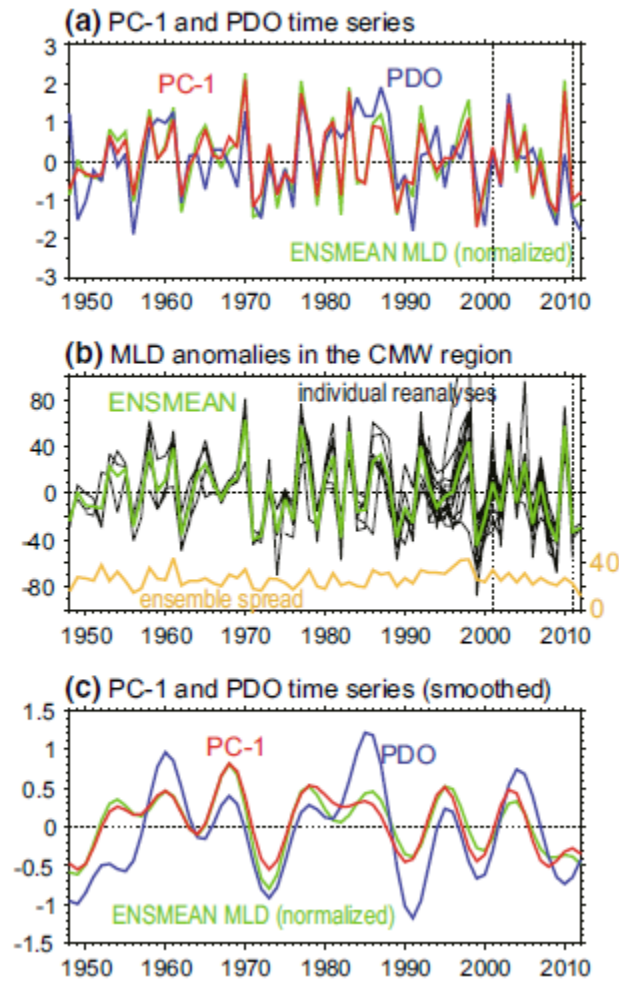
889



890

891 **Fig. 5** (a) Pattern of the EOF-1 for the 2001-2011 period calculated from ensemble mean
 892 wintertime maximum MLDs. Boxes indicate the eastern part of the CMW formation region
 893 (purple), the ESTMW formation region (green), the central Alaskan Gyre (orange) and the Bering
 894 Sea (red). (b) PC-1 for the EOF analyses of the 2001-2011 (red) and 1948-2012 (blue) periods.
 895 (c, d) Same as (a, b) but for EOF-2 and PC-2. The purple box in (c) indicates the STMW formation
 896 region. Note that the EOF projection have been used both to fill spatial gaps and to extend the
 897 time series. Thus, projection values of the PCs are plotted in the region where data are rejected
 898 for the EOF analysis (e.g., in the Okhotsk Sea). Similarly, PCs for 2001-2011 are extended
 899 forward and back to the full 1948-2012 period by projection of the EOF patterns onto the
 900 ENSMEAN interannual anomaly field (thin red line).

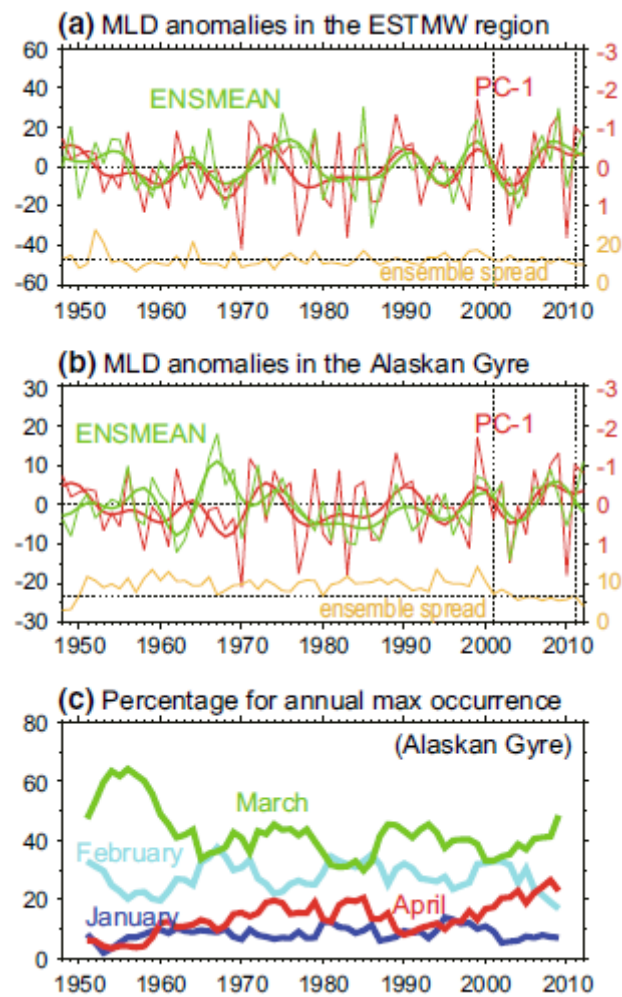
901



902

903 **Fig. 6** (a) PC-1 (red) and the wintertime PDO time series (blue). For the PC-1, projected values
 904 of the EOF-1 pattern are also plotted for the other period of the EOF analysis (2001-2011). Green
 905 line denotes the interannual MLD anomalies of ENSMEAN averaged over the eastern part of the
 906 CMW formation region (180° - 160° W, 32° N- 42° N; purple box of Fig. 5a; left axis) and
 907 normalized by their standard deviation. (b) Time series of the interannual MLD anomalies
 908 averaged over the eastern part of the CMW formation region (left axis) for the individual
 909 reanalyses (17 black lines) and ENSMEAN (green line). In addition, time series of the ensemble
 910 spread averaged over the same region are plotted (yellow line; right axis). Units are in meter. (c)
 911 Same as (a) but smoothed by a band-pass filter for the 7-54 year band. Note that the lower
 912 frequencies are cut in order to eliminate the trends of the time series.

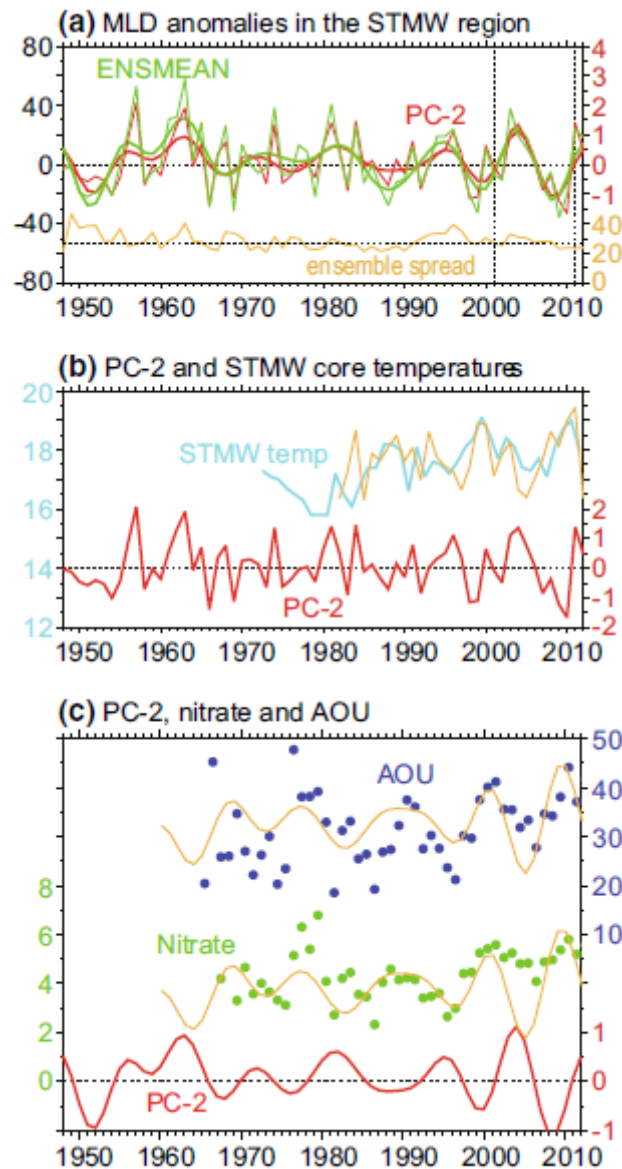
913



914

915 **Fig. 7** Raw (thin) and 7-year low-pass filtered (thick) time series of the interannual anomalies of
 916 the wintertime maximum MLDs averaged over the ESTMW formation region (145°W - 135°W ,
 917 22°N - 30°N ; green box of Fig. 5a; left axis) for ENSMEAN (green) and PC-1 (red; right axis in
 918 red with the numbers upside down). Time series of the ensemble spread averaged over this region
 919 (yellow; right axis in yellow). (b) Same as (a) but for the central Alaskan Gyre (160°W - 140°W ,
 920 45°N - 53°N ; orange box of Fig. 5a). (c) Time series of percentages of each month for the
 921 occurrence of the annual maximum MLDs in the central Alaskan Gyre. All the 17 reanalyses are
 922 used.

923

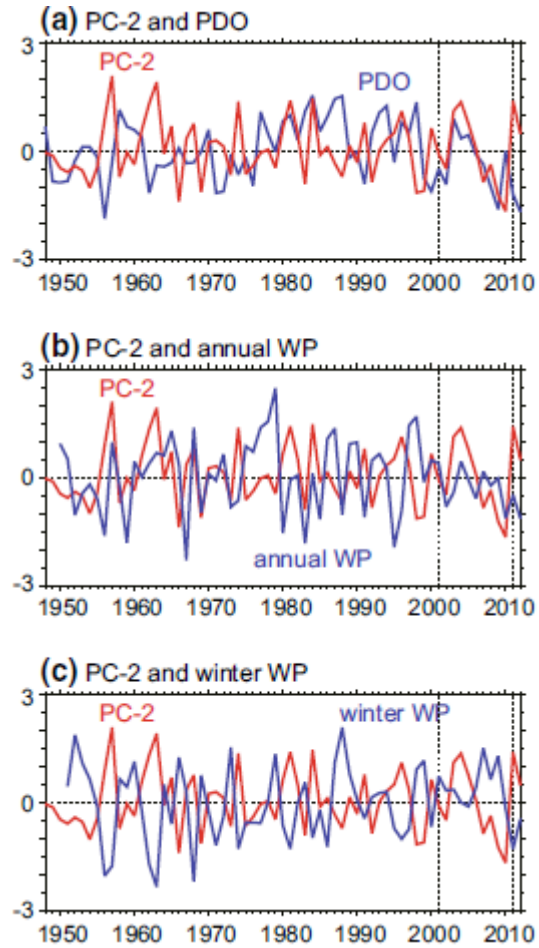


924

925 **Fig. 8** (a) Same as Fig. 7 but for the STMW formation region (140°E - 160°E , 28°N - 36°N ; purple
 926 box of Fig. 5c) and PC-2. (b) PC-2 (red; right axis) and summertime temperatures in the STMW
 927 core at 137°E (light blue; left axis). (c) PC-2 (red; right axis in red) and the annual mean values
 928 of nitrate concentrations (green; left axis; units in $\mu\text{mol}/\text{kg}$) and AOU (blue; right axis in blue;
 929 units in $\mu\text{mol}/\text{kg}$) on the $25.2\sigma_{\theta}$ surface between 28°N and 32°N along the 137°E line. The
 930 summertime temperatures and annual mean nitrate concentrations and AOU are plotted with a
 931 forward offset of half a year. Yellow lines in (c, d) denote the unfiltered/filtered PC-2 but inverted

932 and lagged by 1.5 year.

933

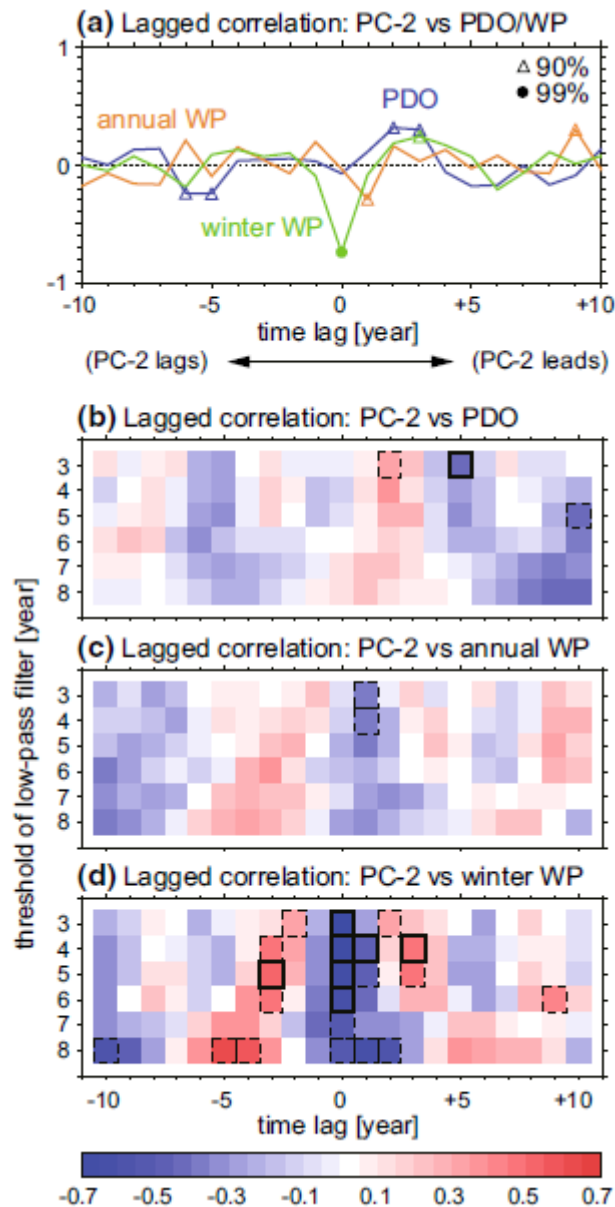


934

935 **Fig. 9** Comparison of the PC-2 (red) with the time series of the annual PDO (a), annual WP (b)

936 and wintertime WP (c) indices (blue).

937

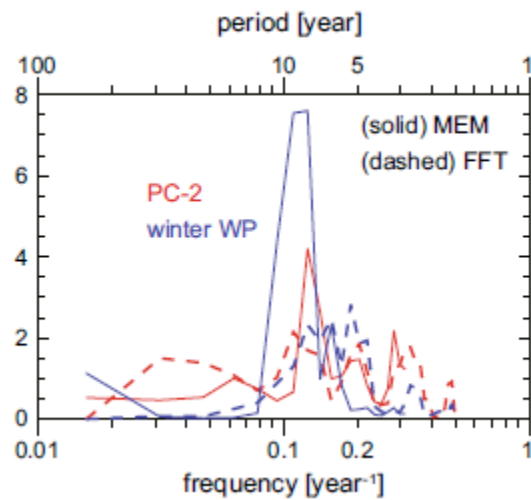


938

939 **Fig. 10** (a) Lagged correlation of the PC-2 with the time series of the PDO (blue), annual WP
 940 (yellow) and wintertime WP (green) indices. Positive (negative) lags indicate the lead (delay) of
 941 the PC-2 over the PDO/WP index. Triangle (circle) indicates the value at a 90% (99%) confidence
 942 level. (b) Lagged correlation between the low-pass filtered time series between the PC-2 and PDO
 943 index depending on the time lag (x-axis) and the number of years of the low-pass filter (y-axis).
 944 Dashed (solid) box indicates the value at a 90% (99%) confidence level. Note that the degree of
 945 freedom changes due to both the decrease in the analyzed period when considering a time lag,

946 and to the filtering of the high frequent variations. (c, d) Same as (b) but for the annual and
 947 wintertime WP indices, respectively.

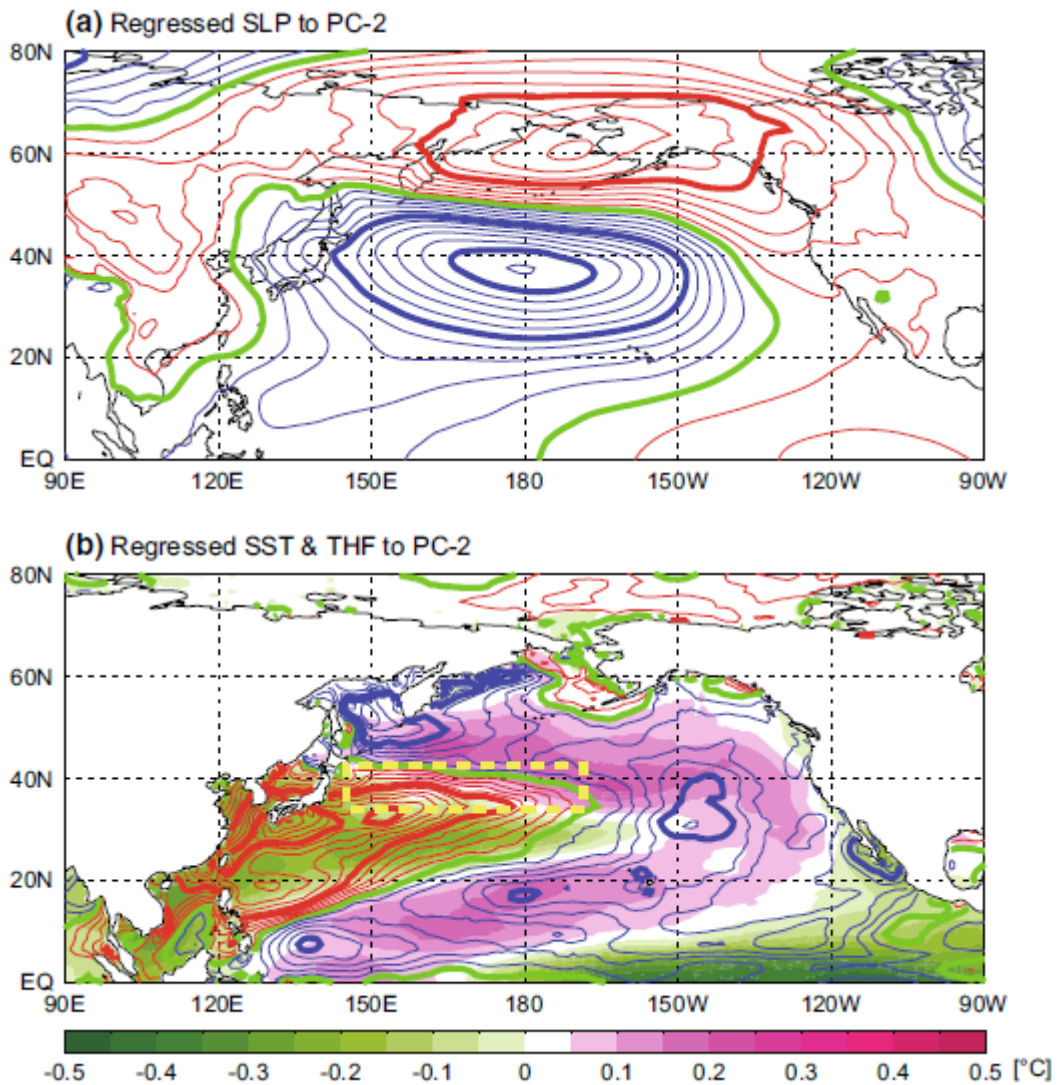
948



949

950 **Fig. 11** Power spectra for the PC-2 (red) and the wintertime WP index (blue) for the 1948-2012
 951 period. Solid lines are based on the maximum entropy method (with the number of poles of the
 952 approximation of 20; see Press et al. 1992). Dashed lines are based on the fast Fourier transform
 953 method. 3-point running mean are taken for the latter.

954



956 **Fig. 12** (a) Regressed SLP pattern to the PC-2. Contour intervals are 0.2 hPa. (b) Regressed SST
 957 (shade) and THF (contour; 2 W/m² intervals) patterns to the PC-2. The JRA-55 and COBE-SST
 958 dataset are used. Blue (red) lines denote contours of negative (positive) values. Zero contours are
 959 indicated by green lines. Yellow box in (b) indicate the Kuroshio Extension region approximately.
 960